Acta Materialia 115 (2016) 333–346

Contents lists available at ScienceDirect

Acta Materialia

journal homepage: www.elsevier.com/locate/actamat

Full length article

On the process of co-deformation and phase dissolution in a hard-soft immiscible Cu–Co alloy system during high-pressure torsion deformation

A. Bachmaier [a, b, *], J. Schmauch [c], H. Aboulfadl [d], A. Verch [e], C. Motz [a]

[a] Chair of Materials Science and Methods, Saarland University, Saarbrücken, Germany
[b] Erich Schmid Institute of Materials Science, Austrian Academy of Sciences, Jahnstrasse 12, Leoben, Austria
[c] Experimentalphysik, Saarland University, Saarbrücken, Germany
[d] Chair of Functional Materials, Saarland University, Saarbrücken, Germany
[e] INM-Leibniz Institute for New Materials, Saarbrücken, Germany

ARTICLE INFO

Article history:
Received 26 March 2016
Received in revised form
31 May 2016
Accepted 3 June 2016
Available online 14 June 2016

Keywords:
Severe plastic deformation
Composites
Mechanical alloying
Microstructure
Atom probe tomography

ABSTRACT

In this study, dual phase Cu–Co composites with a total immiscibility in the solid state and a very different initial phase strength are deformed by severe plastic deformation. Nanocrystalline supersaturated solid solutions are reached in all Cu–Co composites independent of the initial composition. The deformation and mechanical mixing process is studied thoroughly by combining scanning electron microscopy, transmission electron microscopy, three-dimensional atom probe tomography and nano-indentation. The indentation hardness of the Cu and Co phase and its evolution as a function of the applied strain is linked to deformation and mechanical mixing process to gain a better understanding how the phase strength mismatch of the Cu and Co phase effects the amount of co-deformation and deformation-induced mixing. Our results show that co-deformation is not a necessary requirement to achieve mechanical mixing.

1. Introduction

The high level of interest on nanostructured materials with tailored properties for structural and functional applications is still continuing [1–3]. Top-down processing methods such as severe plastic deformation (SPD) are of practical importance if bulk quantities of nanostructured materials are required [4]. In addition to significant grain refinement, the microstructure that evolves after SPD of dual or multiphase materials often contains non-equilibrium phases, for example, supersaturated solid solutions, metastable crystalline and amorphous phases [5–12]. Obtaining supersaturated solid solutions in alloy systems, which are immiscible in equilibrium at ambient temperatures, is often the explicit aim during the SPD process since materials with non-equilibrium microstructures have proven the potential to achieve outstanding mechanical and physical properties [13–22].

The deformation mechanisms of dual or multiphase materials during SPD depend strongly on the strain path (hence the used SPD method) and initial microstructure (phase volume fractions and initial size and shape of the components). Considering co-deformation and subsequent deformation-induced mechanical mixing, the mechanical properties, in particular the yield stress or the yield stress difference as well as the work-hardening of the individual phases of the composites, are especially important [5–7,23–25]. From mechanical alloying during ball milling it is well-established that alloying elements must co-deform for deformation-induced mixing to occur, which basically means that elements with similar mechanical properties need to be combined [26–29]. Therefore, the ideal combination of materials are two ductile materials. If ductile-brittle components are combined, alloying during ball milling is unlikely to occur if the brittle component has a negligible or no solid solubility in the ductile matrix component [30]. The same applies to brittle-brittle components without mutual solid solubility [27,31].

In this study, Cu–Co composites with three compositions (Cu-

* Corresponding author. Erich Schmid Institute of Materials Science, Austrian Academy of Sciences, Jahnstrasse 12, Leoben, Austria.
E-mail addresses: andrea.bachmaier@oeaw.ac.at (A. Bachmaier), schmauch@nano.uni-saarland.de (J. Schmauch), h.aboulfadl@mx.uni-saarland.de (H. Aboulfadl), andreas.verch@leibniz-inm.de (A. Verch), motz@matsci.uni-sb.de (C. Motz).

http://dx.doi.org/10.1016/j.actamat.2016.06.010

26 at.%Co, -54 at.%Co and -76 at.%Co) are deformed by high-pressure torsion (HPT) at room temperature. New insights on the structural evolution and phase formations in this immiscible alloy system are presented in this work and complements an earlier work, where only one composition (Cu-26 at.%Co) was studied [32]. For polycrystalline, coarse-grained Cu and Co, yield stresses between 25 and 80 MPa (depending on grain size) for annealed, oxygen-free Cu and 655 MPa for Co (purity 99.9%, annealed for 1 h at 600 °C) are found in literature [33,34]. HPT deformed pure Cu and Co bulk materials or powders further attain a quite different saturation hardness (about 50% difference) in the steady state of HPT deformation, whereby the hardness of Cu is in both cases significantly smaller compared to Co [22,35,36].

The main focus of the present work is the impact of the ratio of a hard phase (Co) to a soft phase (Cu) on co-deformation, the overall microstructural evolution and phase dissolution during HPT deformation. Hence, Cu–Co composites with specific composition (low, medium and high volume fraction of Co), which exhibit an significant, initial high hardness difference, are deformed [32,37]. The literature contains both, experimental and theoretical research, on how the mechanical properties of the phases influence the amount of deformation-induced mixing [29,38–44]. One open question is, however, how the mechanical properties of the individual phases evolve with increasing amount of applied strain and if it is considerably influenced by the phase volume fraction of Co. Therefore, the indentation hardness of the Cu and Co phase is separately monitored as a function of the applied strain by nanoindentation in this study. The indentation hardness evolution of the Cu and Co phase is linked to the general deformation behavior - especially considering the amount of co-deformation - of the composite, the level of deformation-induced mixing and the time to reach phase dissolution and a supersaturated solid solution during HPT deformation. The results show that the deformation and mechanical alloying process is a multi-stage process. Additionally, the formation of a supersaturated solid solution in the Co-rich composites is investigated. The very different initial phase strength of the Cu and Co phase has not that particular importance under HPT conditions and mechanical mixing takes place in the hard Co phase of the Co-rich composites as well.

2. Experimental

Cu–Co composite materials with three compositions (Cu-26/54/76 at.%Co), produced by RHP-Technology (Seibersdorf, Austria), were investigated in this study. In the initial state, the Cu–Co composite material consists of the fcc Cu phase and the hcp Co phase [32,37]. The hardness of the individual Cu and Co phase in the as-fabricated, initial condition is 103 ± 12 HV0.5 and 394 ± 21 HV0.5, respectively [32,37]. The Cu–Co composite materials were HPT deformed at room temperature (1–25 rotations, 5 GPa pressure, 0.2 rotations/minute).

Microstructural characterization was carried out using a scanning electron microscope (SEM) type ZEISS SIGMA VP using back scattered electrons (BSE). Vickers microhardness ($H_{V0.5}$) was measured by three individual indents at each measurement position across the radii of the HPT disks with a distance of 0.25 mm between these measurement positions. Using the mean microhardness value at the lowest applied strain as a reference value ($H_{V\varepsilon 0}$), the relative increase in microhardness, $(H_{V\varepsilon x} - H_{V\varepsilon 0})/H_{V\varepsilon 0}$, for each composite material at each measurement position can be calculated.

Grid nanoindentation experiments as described in Ref. [45] were performed with a cube corner diamond tip in displacement controlled mode using constant loading, hold and un-loading times with a Hysitron TriboIndenter® with the Performech™ controller. The individual indents were made following a quadratic square with 1.0 μm distance spacing between each separate indent. The maximum displacement was set to 50 nm for all indentations to avoid size effects. Subsequently, the frequency plots (normalized histograms) of the measured indentation hardness at each measurement position were analyzed through deconvolution processes as described in detail in Ref. [45]. To give an example, the results of the nanoindentation grid test on the Cu-54 at.%Co material at a low applied strain ($\varepsilon = 55$) are illustrated in Fig. 1. The grid contains 121 individual indentations covering a total area of 10 × 10 μm^2. The outlines of the Co and Cu phase can be reasonably well resolved in the color-coded hardness map (Fig. 1a). When the indentation hardness is plotted as histogram (Fig. 1b), two distinct peaks are visible. The mean value of each peak represents the mean hardness of the respective phase. The first peak, which is assumed to be the Cu phase, has a mean of 2.3 GPa. The second peak, which belongs to the Co phase, has a mean of 4.0 GPa. The area under the curve corresponds to the percentage of all indentations conducted on each phase and can be used as a measure of the surface fraction of each phase, theoretically. However, due to the small area covered by the nanoindentation grid test at each applied strain in this work, alternatively the software program ImageJ was used to determine the area fraction of the Cu and Co phase from BSE images for different amount of applied strains (mean of three individual BSE images with a size of 110 × 80 μm^2 at each position).

Analytical transmission electron microscopy (TEM) investigations including scanning TEM (STEM) and electron energy-loss spectroscopy (EELS) were used to characterize the microstructure of the deformed composite material in more detail. TEM analysis was performed using a cold field emission gun TEM/STEM (JEOL JEM-ARM 200F) at 200 keV. It is equipped with a STEM Cs corrector (CESCOR; CEOS GmbH Heidelberg) and a post-column EELS spectrometer (GIF QuantumER™ from Gatan). For STEM, the annular bright-field (ABF) and annular dark-field (ADF) detector with a camera length of 8 cm was used, resulting in a collection angle range of 45 mrad and 68–280 mrad, respectively. The EELS measurements were carried out with a beam current of 530 pA, a collection semi angle of 10.4 mrad, a spectrometer entrance aperture of 2.5 mm and a dispersion of 0.25 eV/ch.

Atomic scale analysis by atom probe tomography (APT) measurements were performed using a LEAP™ 3000X HR CAMECA™ system. Specimens were prepared by site-specific sample preparations in a dual-beam focused ion beam/SEM workstation using the in-situ liftout technique [46]. To minimize Ga induced damage, a 200 nm thick Pt-cap layer was deposited by electron beam assisted physical vapor deposition at the region of interest, and the final steps during specimen shaping were performed using 2 keV. The specimens were measured in laser pulsing mode (532 nm wavelength at 100 kHz repetition rate with a pulsing energy of 0.5 nJ) and a base temperature of 60 K. APT data was reconstructed using the standard algorithm as described in Ref. [47] and analyzed with the software CAMECA™ IVAS 3.6.8.

3. Results

3.1. Structural characterization

The microstructural evolution of the Cu-26 at.%Co composite as a function of applied strain has earlier been presented in Ref. [32]. Fig. 2 shows the microstructure observed in tangential directions for the Cu-54 at.%Co and the Cu-76 at.%Co composite. Between applied strains of 5–120, a rather inhomogeneous microstructural evolution can be observed in both composites (Fig. 2). After deformation to an applied strain of about 5 and 10, the Cu and Co phase is easy distinguishable in both composites (Fig. 2a and e). The

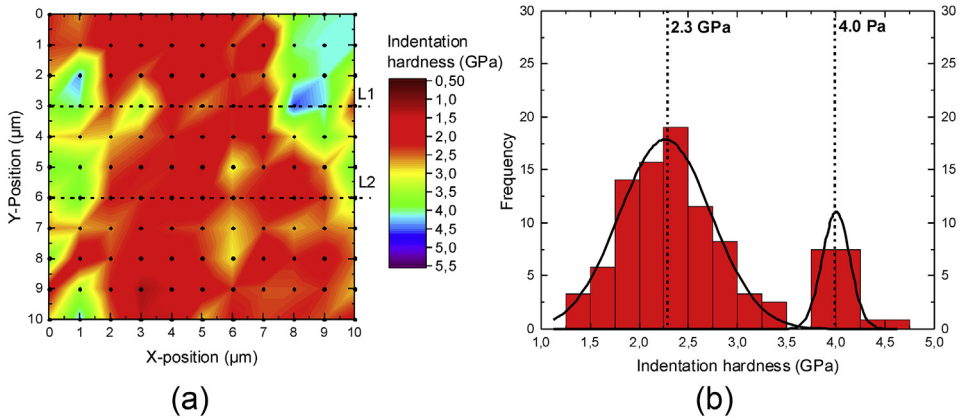

Fig. 1. (a) Indentation hardness map of the Cu-54 at.%Co composite at medium applied strain ($\varepsilon = 55$) as obtained by the grid indentation technique (10 × 10 indents matrix, spacing 1 µm, indentation depth 50 nm) and (b) grid indentation histogram of the dataset illustrating the peaks obtained for the Cu and Co phase and the deconvoluted values of hardness.

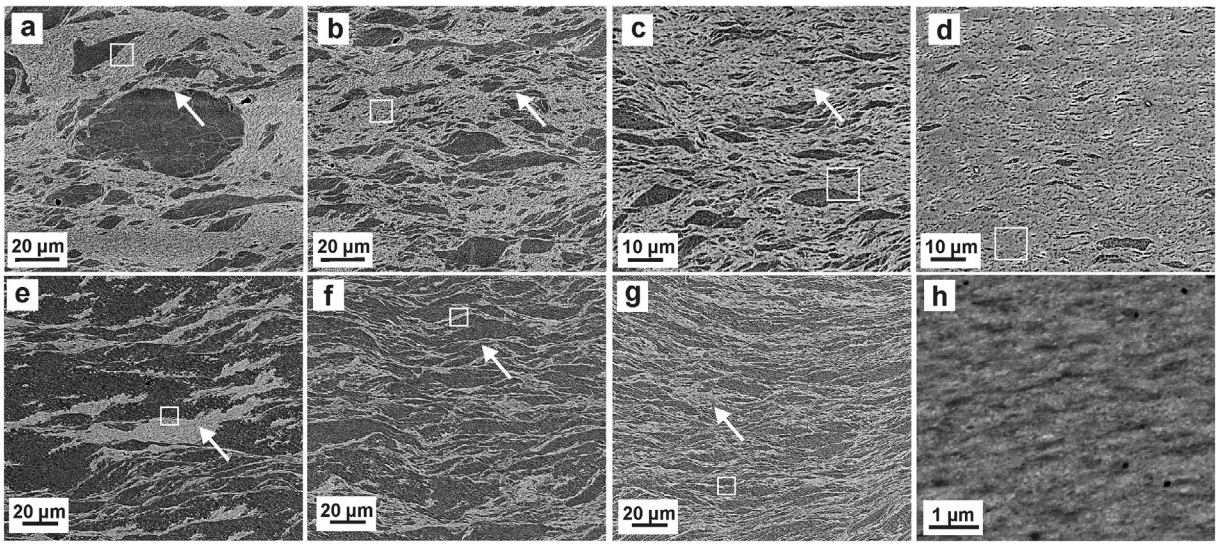

Fig. 2. BSE micrographs taken at different positions of the Cu-54 at.%Co composite at an applied strain of $\varepsilon = 5$ (a), $\varepsilon = 40$ (b), $\varepsilon = 55$ (c), $\varepsilon = 110$ (d) and of the Cu-76 at.%Co composite at an applied strain of $\varepsilon = 10$ (e), $\varepsilon = 25$ (f), $\varepsilon = 100$ (g), $\varepsilon = 120$ (h). Please note the different magnification. The shearing direction is along the lower edge of the BSE micrographs and the same in each micrograph.

magnified BSE micrographs in Fig. 3a and f reveal an ultrafine grained microstructure in the Cu phase at this applied strain, which is comparable to the grain size of the Cu phase in the Cu-rich composite at similar applied strain [32]. A distinct phase boundary between the Cu and Co phases is further visible in Fig. 3a, which is marked by the white dashed line.

In the Cu-54 at.%Co composite (Fig. 2b–d), the evolution of the microstructure as a function of the applied strain is very similar to the Co-26 at.%Co composite despite the almost equal fraction of Co and Cu [32]. Co particles, which have a rather broad size distribution, are randomly distributed in the Cu matrix. Most of the Co particles exhibit an elongation in shearing direction. With ongoing deformation, their size is continuously refined (Fig. 2c–d). It is assumed that the softer Cu undergoes large plastic straining, while the Co particles, which are unable to deform to the same extent, mainly fracture. Fig. 3b and c shows a magnified BSE micrographs at an applied strain of 40 and 55 recorded at positions schematically marked by white arrows in Fig. 2b–c. Compared to the ultrafine grained structure visible in Fig. 3a, the grain size of the Cu phase is reduced by almost half. In vicinity of the Co phase, the grain size is even smaller, which is exemplarily indicated by the dashed white lines in the micrographs. Up to an applied strain of 100–110 (Figs. 2a–d and 3a–c), Co and Cu phases are, however, easily distinguishable in the micrographs with low and high magnification. At an applied strain of 160, distinct Cu and Co phases are no longer clearly resolvable in the SEM and overall grain size is further reduced (Fig. 3d). Dark areas, which are assumed to be Co-rich, are still found at higher magnification (some are marked in Fig. 3d). In the BSE micrograph recorded at an applied strain 440, these contrast variations are reduced and the microstructure appears to be more homogeneous (Fig. 3e).

In the Cu-76 at.%Co composite, the microstructural evolution as a function of the applied strain is different and a rather lamellar microstructure is formed (Fig. 2e–g). Cu and Co are again not deforming to the same amount. While the Cu phase is strongly elongated in shearing direction, the Co phase is less deformed and behaves in a similar way as already observed for the Co phase in the Cu-26 at.%Co and Cu-54 at.%Co composites. As a consequence of the lack of co-deformation, the Cu lamellae are deviating from a strict alignment in shearing direction because they have to follow the

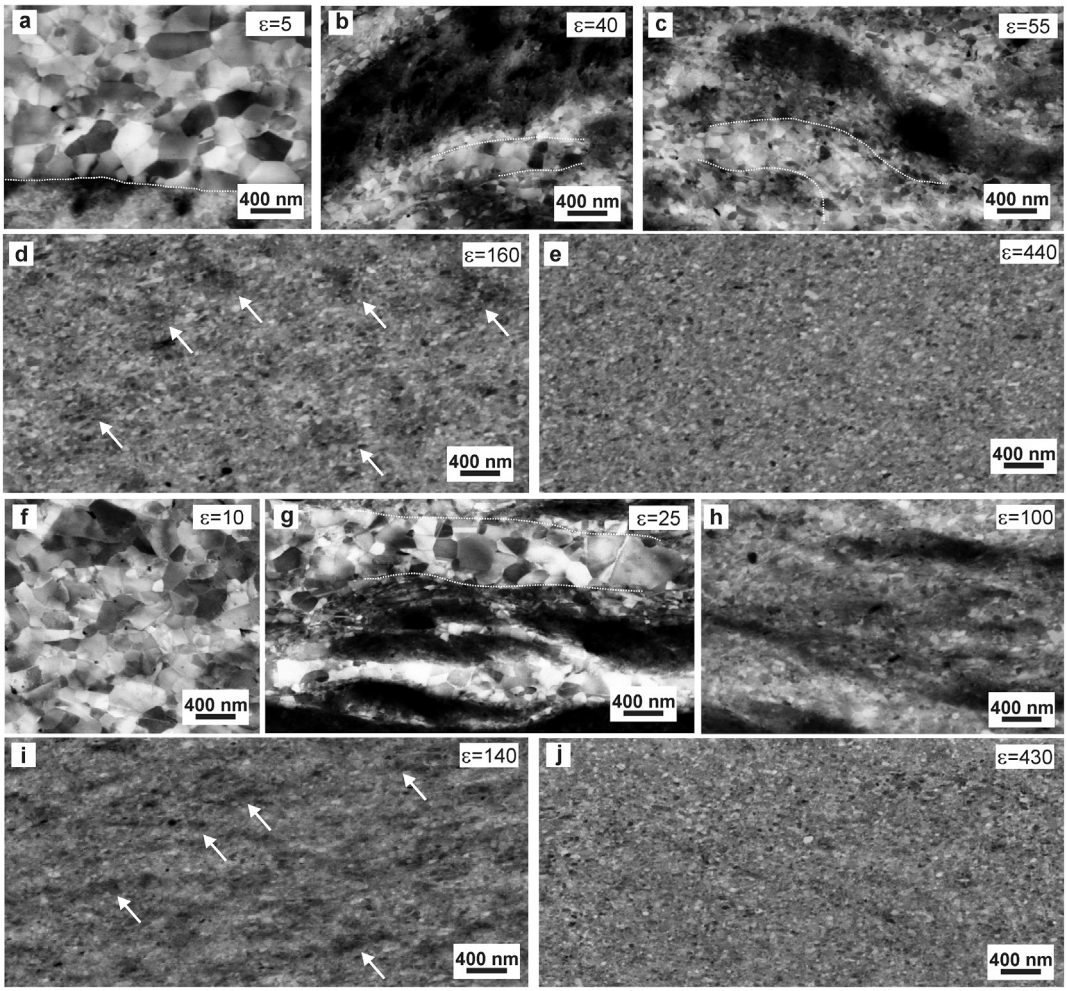

Fig. 3. BSE micrographs of the Cu-54 at.%Co composite at an applied strain of $\varepsilon = 5$ (a), $\varepsilon = 40$ (b), $\varepsilon = 55$ (c), $\varepsilon = 160$ (d) and $\varepsilon = 440$ (e) and the Cu-76 at.%Co composite at an applied strain of $\varepsilon = 10$ (f), $\varepsilon = 25$ (g), $\varepsilon = 100$ (h), $\varepsilon = 140$ (i) and $\varepsilon = 430$ (j) with the same magnification in each micrograph.

shape of the less deformable Co phase. An increase in the applied strain from 10 to 100 refines the size of the Cu lamellae. Inside the Cu lamellae (an example is shown in the magnified BSE micrograph in Fig. 3g), a rather large grain size can be seen at a medium applied strain ($\varepsilon = 25$). Next to the Co phase (indicated by the dashed white lines in the micrograph), a significantly smaller grain size is observed, again. At an applied strain of 100, the grain size in the Cu-rich lamella becomes more evenly and is further strongly refined (Fig. 3h). Although the lamellar microstructure of the Cu-76 at.%Co composite is clearly resolvable up to an applied strain of 100 (Fig. 2e–g), much higher magnification is needed at a little higher applied strain to differentiate between the two phases ($\varepsilon = 120$). In the magnified BSE micrograph (Fig. 2h), alternating, lamellar arranged bright and dark bands, most likely Cu-rich and Co-rich areas, are still distinguishable. The grain size in the bright and dark areas seems to be nearly the same. Bright and dark bands, hence Cu and Co rich areas are even resolvable at an applied strain of $\varepsilon = 140$ (Fig. 3i). Applying further strain ($\varepsilon = 430$) results in a homogeneous microstructure with nanocrystalline grains (Fig. 3j), similar as observed in the Cu-26 at.%Co [32]and Cu-54 at.%Co composites.

3.2. Mechanical characterization

The microstructural evolution of the Cu–Co composite materials is further reflected in their microhardness, which increases as function of the applied strain. As an example, Fig. S1 shows the hardness profile of the Cu-54 at.% Co composite HPT deformed for different number of rotations. Similar hardness distributions have been found for the Cu-26 at.%Co and -76 at.%Co composite [37]. In order to compare the microhardness increase with increasing applied strain, the relative change of the microhardness as a function of applied strain for each composite is plotted in Fig. 4a. As a reference value at each point, the mean microhardness at the lowest applied strain ($HV_{\varepsilon 0}$) is used for the calculation of the relative change, which is exemplary shown in Fig. S1 for an applied strain of 485 (Cu-54 at.%Co composite).

A first glance it seems that all composites show similar hardening characteristics. Initially, the curves ascend quickly but then reach a kind of plateau with few or minor subsequent changes. Fig. 4b depicts an enlarged view of the first part of the hardness plot (grey-shaded area in Fig. 4a) for all composites, in which differences in the hardening behavior of the composites can be revealed. An initial steep increase is characteristic for all three composites. The slope of a linear fit of the first part of the diagram yields 1.0, 1.5 and 3.0 for the Cu-26 at.% Co, -54 at.%Co and -76 at.%Co, respectively. After this first increase, a region of nearly steady microhardness ($10 \leq \varepsilon \leq 60$) follows in the Cu-26 at.%Co composite. Afterwards further distinct hardening is observed until a second region of nearly steady hardness is reached. Such regions with less hardening

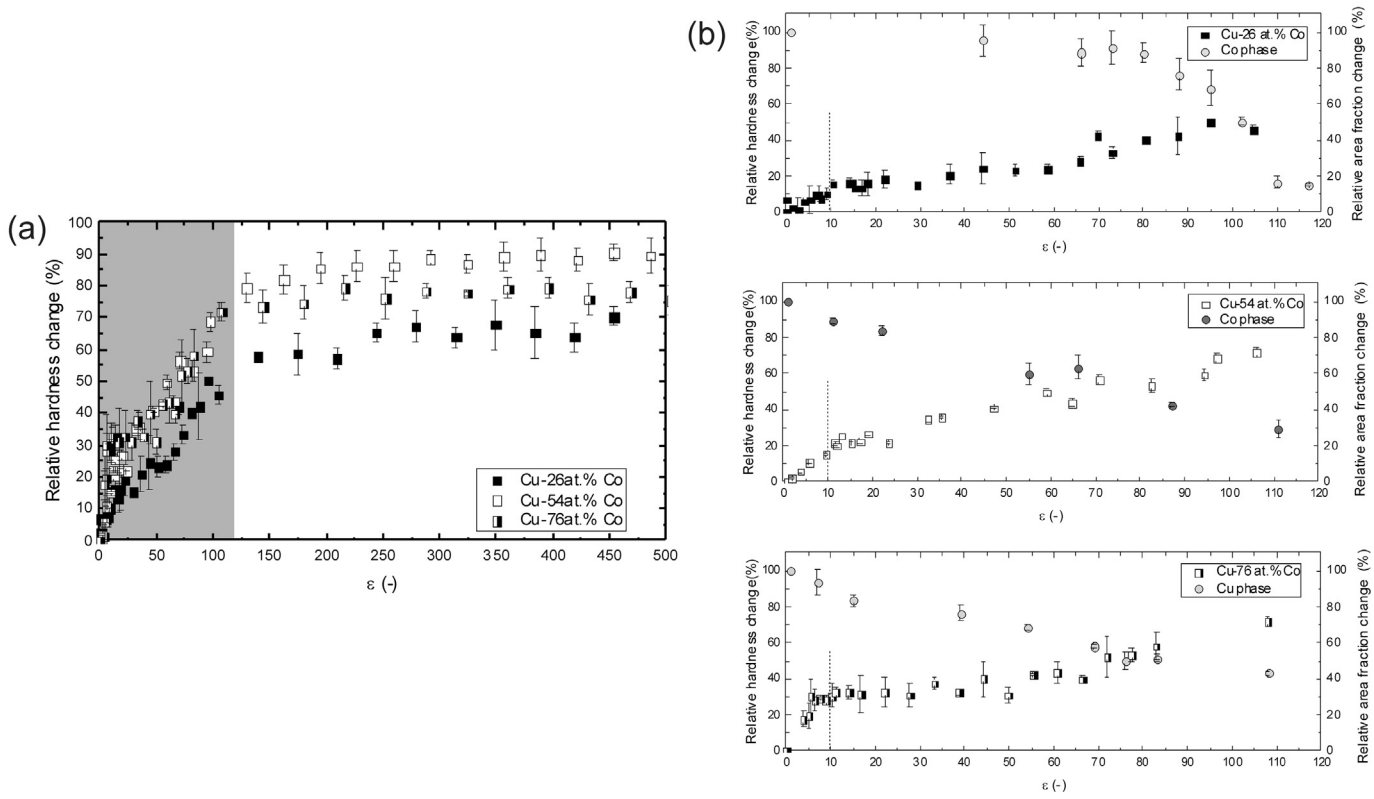

Fig. 4. (a) Relative change of the microhardness as a function of applied strain for each composite, which is calculated by using the mean microhardness at the lowest applied strain ($H_{V\varepsilon 0}$) as a reference value at each point. For example, the relative change at an applied strain of 485 for the Cu-54 at.%Co composite is calculated by $(H_{V\varepsilon 485} - H_{V\varepsilon 0})/H_{V\varepsilon 0}$ with $H_{V\varepsilon 0}$ and $H_{V\varepsilon 485}$ being the mean microhardness at an applied strain $\varepsilon = 0$ and $\varepsilon = 485$ as indicated in Fig. S1. (b) Enlarged view of the relative change of the microhardness (grey-shaded area in (a)) plotted together with the determined area fraction of the Co or Cu phase from BSE micrographs at different applied strains.

seems to be less pronounced in the Cu-54 at.% Co ($12 \leq \varepsilon \leq 25$) and Cu-76 at% Co composite ($10 \leq \varepsilon \leq 40$).

The size of the microhardness indents is, except at very small applied strains, much larger than the characteristic size of the Cu and Co phase. Hence, microhardness testing senses the average response of the composites. On the other hand, if the indentation depth is smaller than the phase size, material properties of each phase can be obtained. To monitor the hardness of the individual Cu and Co phases as a function of the applied strain, a grid nanoindentation technique is used at different positions across the radii of the HPT disks for each composite material [45]. In a large range of applied strains, the indentation depth (50 nm) is smaller than the size of the individual phases, which allows to determine the indentation hardness of either the Cu or the Co phase (results summarized in Table 1). At high applied strains, the size of the individual phases as well as hardness differences are reduced. Therefore, only one peak is observed in the corresponding histograms (referred to as "single peak" indentation hardness in Table 1).

Color-coded hardness maps of the Cu-26 at.%Co composite, which were recorded at different degrees of deformation, are shown in Fig. 5a for selected positions. Similar maps of the Cu-26 at.%Co composite were already published in Ref. [32]. Due to different parameters used in this study, nanoindentation experiments have been repeated in order to facilitate comparison with the results of the Cu-54 at.%Co and Cu-76 at.%Co composite. At low applied strains ($\varepsilon = 10$ and 60), areas with high (Co phase) and low hardness (Cu phase) can be easily distinguished in hardness maps. In contrast, the histograms of the hardness data obtained at applied strains of $\varepsilon = 275$ and 370 show only one peak with a mean of 1.9 GPa and 2.0 GPa. The corresponding hardness map in Fig. 5a reveals, however, that small areas with an enhanced hardness still exist at an applied strain of $\varepsilon = 275$. Even at an applied strain of $\varepsilon = 370$, very small areas with higher hardness are still visible. Their size is, however, reduced.

Table 1
Mean indentation hardness (GPa) of the Cu and Co phase of the Cu-26,-54 and-76 at.% Co composite obtained from normalized histograms at different amounts of applied strain (ε). "Single peak" corresponds to the mean indentation hardness value, which is obtained if only one peak is observed in the normalized histograms.

	ε (−)	Indentation hardness (GPa)		
		Cu	Co	Single peak
Cu-26 at.% Co	10	1.0 ± 0.06	3.4 ± 0.13	
	60	1.1 ± 0.03	3.3 ± 0.05	
	100	1.3 ± 0.06	3.6 ± 0.05	
	275			1.9 ± 0.03
	370			2.0 ± 0.05
	430			1.9 ± 0.07
Cu-54 at.% Co	5.10	1.5 ± 0.04	4.0 ± 0.01	
	40	2.2 ± 0.14		
	55	2.3 ± 0.03	4.0 ± 0.02	
	85	2.6 ± 0.06		
	110			3.0 ± 0.02
	165			3.2 ± 0.02
	440			3.3 ± 0.02
Cu-76 at.% Co	10	1.9 ± 0.12	4.2 ± 0.09	
	25	2.5 ± 0.06	3.8 ± 0.02	
	35	2.7 ± 0.13	3.9 ± 0.02	
	100	3.2 ± 0.09	4.0 ± 0.19	
	140			3.3 ± 0.06
	270			3.7 ± 0.02
	430			3.9 ± 0.02

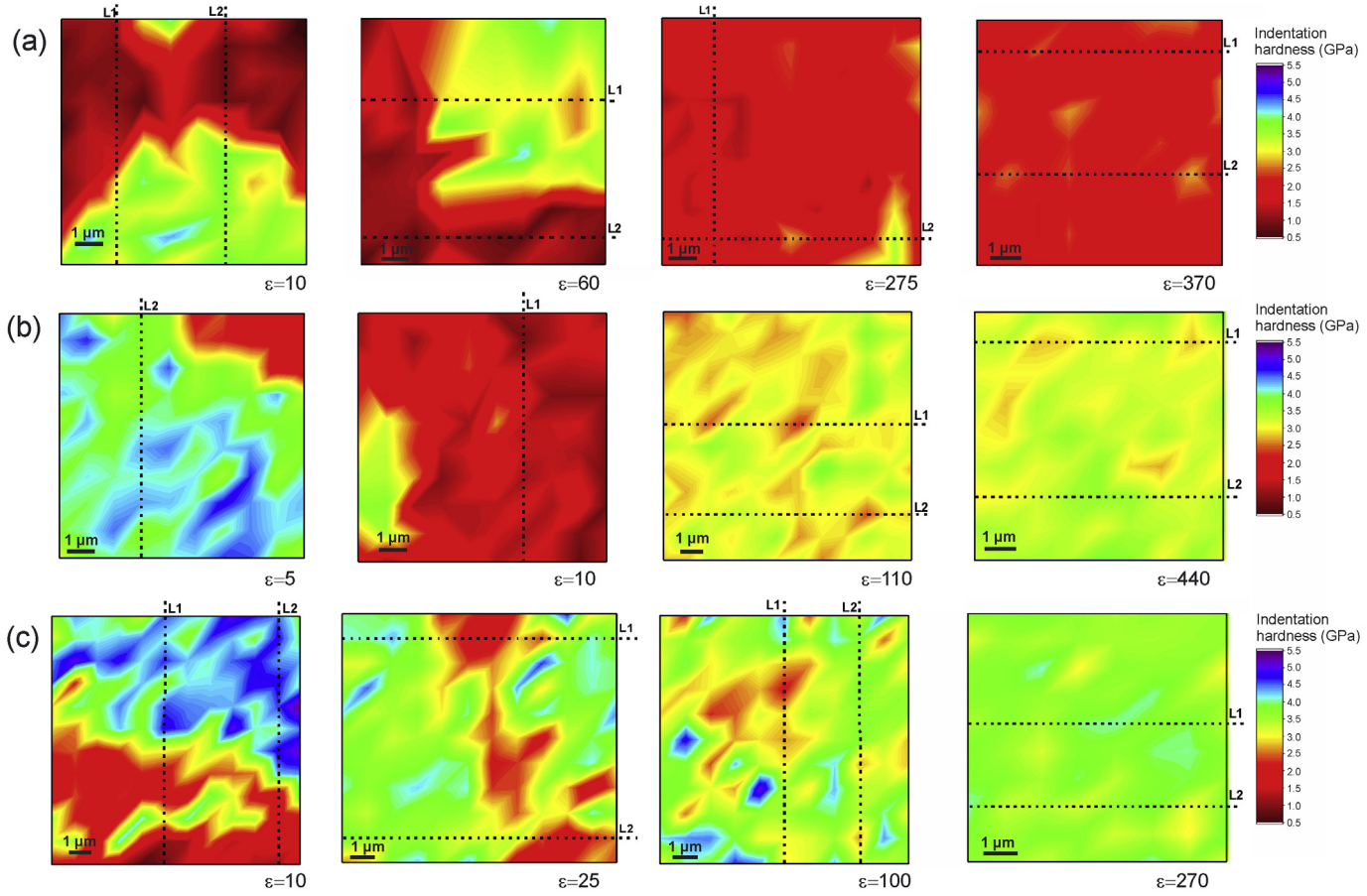

Fig. 5. Color-coded maps of the measured indentation hardness of the Cu-26 at.%Co composite (a), the Cu-54 at.%Co composite (b) and the Cu-76 at.%Co composite (c) at different amounts of applied strain (as indicated in the maps). The indentation hardness values are displayed in GPa.

The white squares in Fig. 2a–d schematically mark regions representing the areas of the Cu-54.at%Co composite investigated by the nanoindentation grid technique (Fig. 5b). At the smallest amount of applied strains ($\varepsilon = 5$ and 10), Cu and Co regions are visible, which have a hardness of 1.5 GPa and 4.0 GPa, respectively (Table 1). In Fig. 1, the hardness map of the Cu-54.at%Co composite obtained at a medium applied strain ($\varepsilon = 55$) is shown. The indentation grid is positioned such that it covers a Cu-rich area between two Co-rich areas. The peak hardness of the Cu and Co phase obtained from the corresponding histogram is 2.3 GPa and 4.0 GPa (Table 1). At higher applied strains, the histograms of the measured indentation hardness data display only one peak. The homogeneous hardness distribution is further illustrated in Fig. 5b.

At a small applied strain ($\varepsilon = 10$), the hardness map obtained from the composite with the highest Co content (Cu-76 at.%Co) as well as the measured indentation hardness of the Cu and Co phase are similar to those observed in the composites with lower Co content (Fig. 5c, Table 1). At an applied strain of $\varepsilon = 25$, the indentation grid is placed across a Cu band in the Co matrix (similar microstructure as shown and marked by the white square in Fig. 2f), from which hardness values of 2.5 GPa (Cu) and 3.8 GPa (Co) are obtained. At a higher applied strain ($\varepsilon = 100$), the indentation grid is again positioned across a Cu band as schematically marked in Fig. 2g. Mean values of 3.2 GPa (Cu) and 4.0 GPa (Co) are measured at this position. With ongoing deformation, the hardness differences diminish further (one example for $\varepsilon = 270$ shown in Fig. 5c).

The mean indentation hardness values, which could be separately obtained for the Cu and Co phase, are furthermore plotted in Fig. 6a as a function of the applied strain. From the plot it is evident that the indentation hardness of the Co phase stays rather high and constant for each composite type (average of 3.8 ± 0.3 GPa considering all data, which is indicated by dashed line). When it comes to the Cu phase, the picture is entirely different. In the Cu-26 at.%Co composite, the indentation hardness of the Cu phase increases a little with increasing applied strain (from 1.0 GPa to 1.3 GPa at an applied strain of 10 and 100, respectively). By comparison, the indentation hardness of the Cu phase in the Cu-54 at.%Co and Cu-76 at.%Co composite increases to a much larger extent.

In order to highlight hardness differences and make them apparent, even if only one peak is observed in the corresponding histograms, the indentation hardness measured along vertical or horizontal lines across features with very low or high hardness in the various hardness maps (marked in Figs. 1 and 5) is additionally plotted in Fig. 7. The difference between the highest and lowest measured hardness value is further highlighted by the grey shaded area in each graph. The indentation hardness measured along the lines at the lowest applied strain ($\varepsilon = 5$–10) reflect the high hardness difference between the Cu and Co phase in each composite (Fig. 7a–c). At an applied strain of 275, line L2 intersects the area of enhanced hardness in the Cu-26 at.%Co composite, which displays a maximum indendation hardness (H_{max}) of 3.4 GPa. The Cu phase has a rather constant indentation hardness at this applied strain along the selected line L1 with a minimum indentation hardness (H_{min}) of 1.4 GPa. When not considering the mean, but

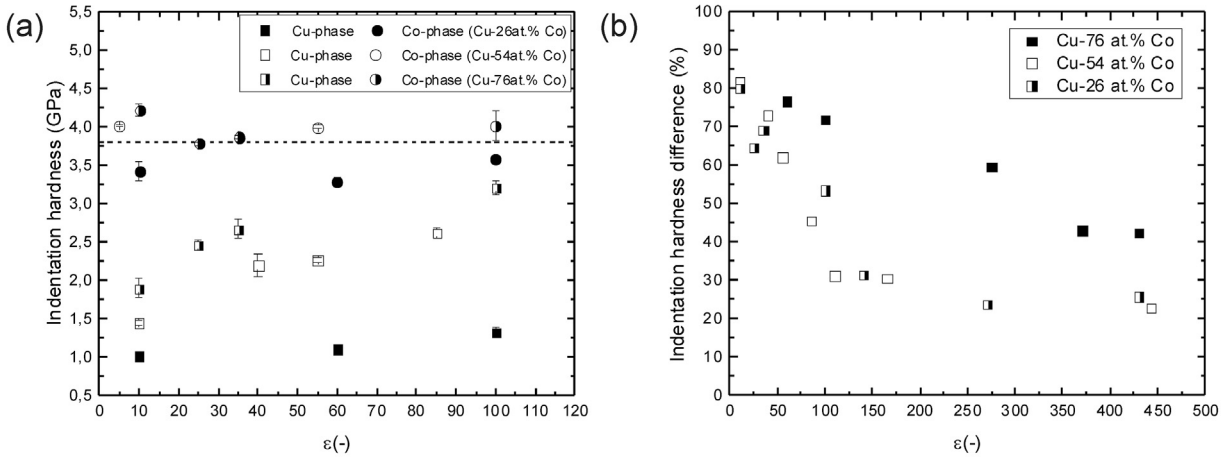

Fig. 6. (a) Mean indentation hardness of the Cu and Co phase as a function of applied strain ($\varepsilon \leq 120$) and (b) Indentation hardness difference between the Cu and Co phase as a function of applied strain for the Cu-26 at.%Co, Cu-54 at.%Co and Cu-76 at.%Co composite.

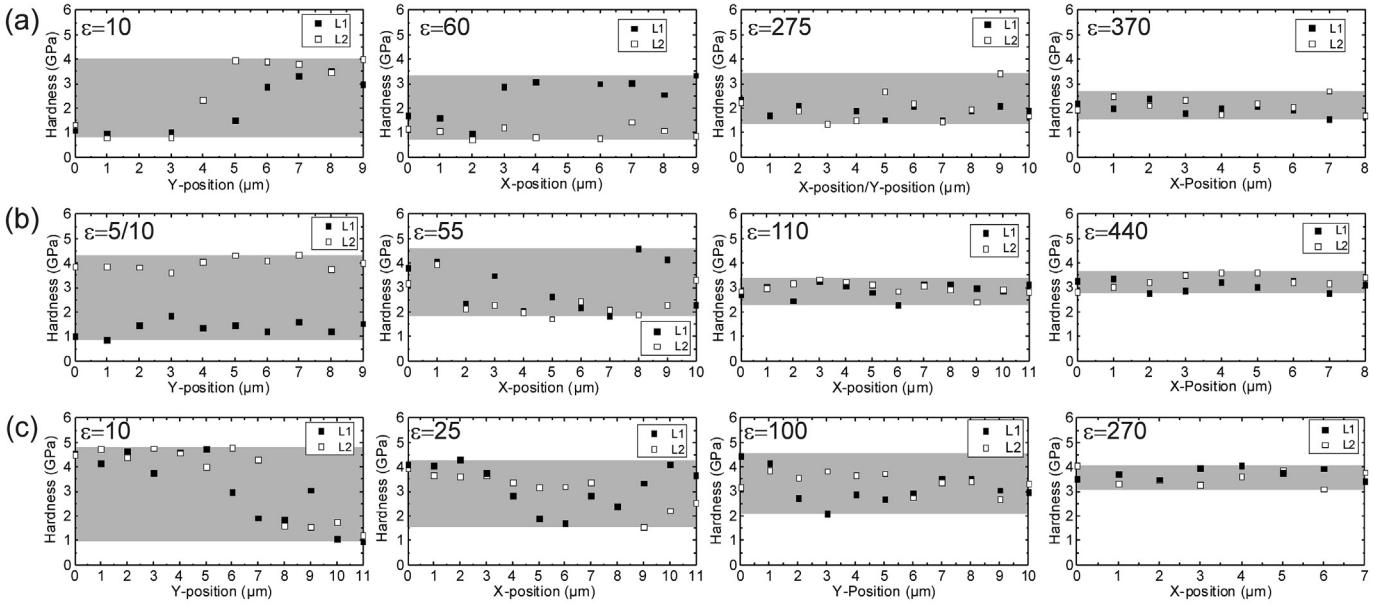

Fig. 7. Indentation hardness of the Cu-26 at.%Co (a), Cu-54 at.%Co (b) and Cu-76 at.%Co (c) composite obtained along vertical or horizontal lines, which are marked (L1, L2) in the corresponding hardness maps in Fig. 1 and 7. The grey shaded areas highlights the difference between the measured minimum and maximum hardness values.

these minimum and maximum indentation hardness values, a hardness difference at each position can be calculated by $(H_{max} - H_{min})/H_{max}$ for the three composite types (Fig. 6b). In the Cu-26 at.%Co composite, a high hardness difference (about 70–80%) between the Cu and Co phases is obtained, which reduces only slightly at low and medium applied strain ($\varepsilon \leq 100$). Even at an applied strain of 275, the calculated hardness difference is still 60%. Further deformation, however, reduces the differences, which reach a minimum of 42% at an applied strain of 430.

Although the mean hardness of the Cu phase in the Cu-54 at.%Co composite at an applied strain of 55 is quite high (2.3 GPa), the hardness in the center of the Cu phase is still lower (Fig. 7b). Hence, a quite high hardness difference (62%) is measured, which is quickly reduced to 31% ($\varepsilon = 110$) and 23% ($\varepsilon = 440$) with ongoing deformation (Fig. 6b).

A similar trend is observed for the Cu-76 at.%Co composite: At an applied strain of 25, line L1 and L2 intersect both, areas with high and low hardness, visible in the hardness map in Fig. 5c. Considering once more the minimum and maximum, it yields a difference of 65%. At a higher applied strain ($\varepsilon = 100$), a minimum and maximum of 2.1 GPa and 4.5 GPa are measured along line L1, which crosses Cu and Co phases (54% difference). In the same map, along line L2, the difference is, however, smaller (32%) and continuously decrease with increasing deformation (Fig. 6b).

In addition to the relative change of the microhardness, the area fraction of the Co or Cu phase is determined from BSE micrographs. To facilitate a comparison, the data is normalized to the initial value and the relative change of the area fraction is plotted in Fig. 4b. The Co phase fraction in the Cu-26 at.%Co composite decreases only slightly to 89% at an applied strain of 65. Afterwards, it reduces more quickly to 50% ($\varepsilon = 100$) and less than 20% at higher applied strains. In contrast, a continuous and larger reduction of the Co phase area fraction is observed in the Cu-54 at.%Co composite. At an applied strain of 55, for example, only one third of the area belongs to the Co phase (60% reduction). At an applied strain of 110, the area fraction is further quickly reduced to 29%. Similar behavior is

revealed for the Co-rich composite: the area fraction of the Cu phase in the Cu-76 at.%Co composite reduces slightly slower compared to the Cu-54 at.%Co composite, but more steadily if compared with the Cu-26 at.%Co composite (to 69%, 50% and 43% at an applied strain of 55, 75 and 110, respectively). The decreasing amount of Cu and Co phase in the composites might be taken as a rough estimate for the dissolution of the respective element into the other phase of the composite. Based on this assumption, the dissolution of Cu or Co seems to proceed faster in the composites containing the higher fraction of the hard Co phase and correlates quite well with relative hardness increase. It should, however, be noted that due to the resolution limit of the SEM, nanoscaled particles cannot be resolved and are therefore not detected by the image analysis software.

3.3. Characterization of mechanical alloying

To measure the Cu and Co distribution and confirm their possible dissolution in the other phase of the composite at atomic scale - especially in the regions near the phase boundaries, which display a smaller Cu grain size (see Fig. 3b,c,g) - site specific APT specimens have been prepared from the Cu phase in the Cu-76 at.% Co composite at a relatively small applied strain ($\varepsilon = 30$). The white lines in Fig. 3g mark regions represent the volume investigated by APT. In all reconstructed volumes, Cu atoms are displayed in blue and Co atoms are illustrated in red. Fig. 8a shows the top-view of a reconstructed volume, in which both phases, Co and Cu, are visible. The blue isoconcentration surface, corresponding to 54 at.% Cu, displays a Cu-rich zone inside the Co phase region. 1D-concentration profiles obtained from two region-of-interests (marked as A and B with the analysis direction indicated by the arrows) reveal that at this position nearly no Co atoms can be detected in the Cu phase region. This was further confirmed by the local composition measurements in a larger sampling region ($20 \times 50 \times 25$ nm^3) within the Cu-rich region which showed 96.2 at.% Cu (±0.1 at.%) and 3.7 at.% Co (±0.1 at.%). By contrast, the concentration mapped across the Cu-rich zone inside the Co phase (cylinder A) shows a Cu concentration of ~60 at%. However, the concentration of Cu atoms between the Cu phase and the Cu-rich zone is nearly zero along this mapped region. In the region of the Co phase located behind this Cu-rich zone (mapped in 1-D concentration profile B), a substantial amount of Cu (up to 30 at.%) is dissolved. Fig. 8b–c shows a reconstructed volume (with side and top-views) of the same Cu-76 at.%Co composite sample prepared from a position ~3 μm away from the specimen shown in Fig. 8a, within the Cu phase region. In both views, the red isodensity surface corresponds to 14 Co atoms nm-3. In the reconstructed volumes, Cu- and Co-rich regions are again identifiable. In contrast to the previously shown almost Co free Cu phase, regions enriched by Co are now clearly visible inside the Cu phase. Significantly higher Co concentrations are measured in the mapped region and a small zone with strong Co enrichment (~40 at.% Co) is further observable in the Cu phase (Fig. 8d). Simultaneously, up to 30 at% Cu are dissolved in the Co-rich region. The higher amount of Co, which is dissolved in the Cu phase at this APT specimen position, was further confirmed by local composition measurements from the Cu-rich region at this position, which showed 90.0 at.% Cu (±0.1 at.%) and 9.8 at.% Co (±0.1 at.%) ($20 \times 25 \times 50$ nm^3 sampling region).

From BSE micrographs, homogeneous microstructures are apparent in the saturation region (Fig. 3e and j). TEM analysis of the composites confirms the nanocrystalline microstructures for all compositions. The formation of supersaturated solid solutions has been recently validated by APT and EELS analysis in the Cu-26 at.% Co composite [32]. Evaluation of selected area diffraction patterns,

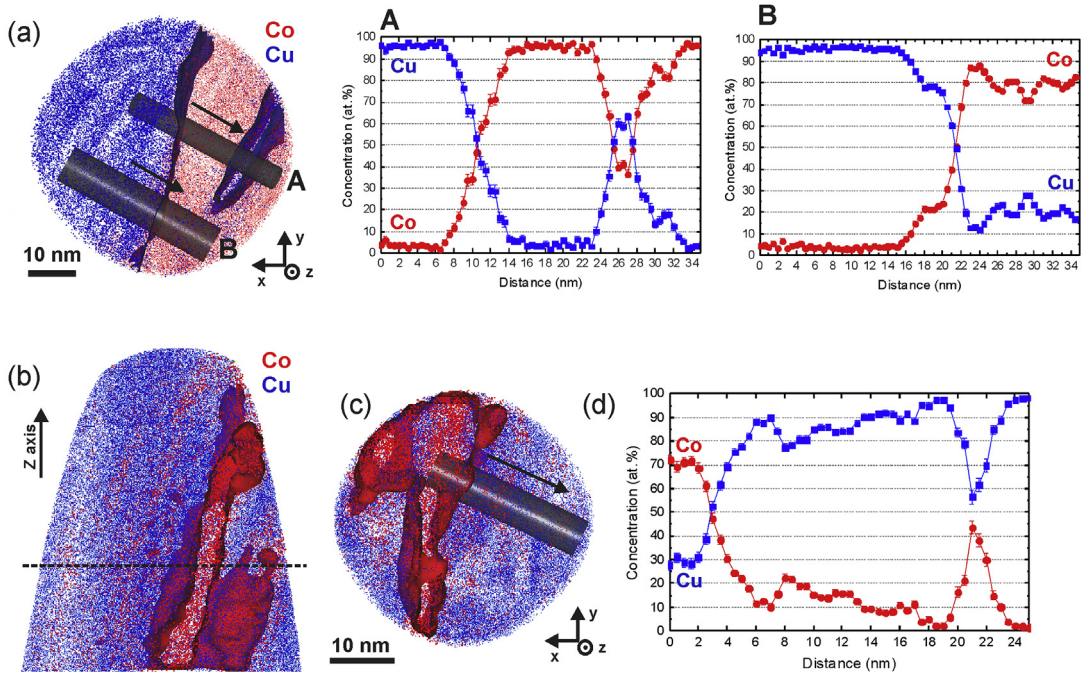

Fig. 8. APT reconstructions of a Cu phase in the Cu-76 at.%Co composite sample deformed to an applied strain of about 30. (a) Tomographic slice (top-view with a thickness of 10 nm), in which the blue isoconcentration surface corresponds to 54 at.%Cu. Cu atoms are displayed twice as large as Co atoms. Size of sampling cylinders: Ø 5 nm × 35 nm (A), Ø 8 nm × 35 nm (B), thickness of sampling volume in A and B: 0.5 nm 1D-concentration profiles are computed along the region-of-interest marked as "A" and "B". (b) Tomographic slice (side-view with a thickness of 10 nm), in which the red isodensity surface corresponds to 14 Co atoms nm^{-3}. Co atoms are displayed twice as large as Cu atoms. (c) Top-view of a tomographic slice along the z-axis of reconstruction (position marked in (b) by dotted line) with a thickness of 10 nm. (d) 1D-concentration profile plotted along the marked region-of-interest. Size of sampling cylinder: Ø 6 nm × 25 nm, thickness of sampling volume: 0.5 nm. (For interpretation of the references to color in this figure legend, the reader is referred to the web version of this article.)

that display only one set of diffraction rings for the Cu-54 at.%Co and Cu-76 at.%Co composite, further suggests that Cu–Co solid solutions are formed in the Co-rich composites. To confirm the formation of Cu–Co solid solutions in the Co-rich composites, further investigations using APT and EELS analysis are conducted at the highest applied strain (i.e. in the saturation region) in both composites. The advantage of EELS is the larger volume which can be analyzed compared to APT. Hence, information about the homogeneity of the Cu and Co distribution on a larger length scale can be obtained and it is further possible to exclude that Cu-or Co-rich grains still exist in the microstructure. As thin as possible TEM specimens (~20–80 nm) were used to exclude 2D-projection effects on the composition to a large extent.

In Fig. 9a, an ABF and ADF STEM image (both taken at the same position) of the Cu-54 at.%Co composite at an applied strain of 440 are shown. EELS line scan analysis was carried out to determine the local chemical distribution of Cu and Co in several grains at different positions of the Cu-54 at.%Co sample. In Fig. 9b, two of these EELS measurements, which are obtained along line 1 and line 2 marked in the STEM images in Fig. 9a, are exemplarily shown. For the concentration profile along line 1 and 2, 109 and 49 measurements with 1.0 nm spacing are conducted, respectively. Line 1 crosses several grains, most of them have a size less than 50 nm (see ABF STEM image). Nonetheless, no distinct Cu- or Co-rich grains can be identified and a quite uniform distribution of Cu and Co is measured. Along line 2, the Co and Cu concentration profile looks very similar.

Additional correlative APT analysis is conducted to investigate the distribution of Cu atoms in the nanostructure of the Cu-76 at.% Co composite at the highest amount of applied strain ($\varepsilon = 430$). As shown in the three-dimensional reconstructions for two analyzed volumes, which are obtained from two different APT specimens, the distribution of the Cu atoms appears visually homogeneous (Fig. 9c–d). The average Cu concentration in these volumes is 21.8 ± 0.1 at% (Fig. 9c) and 24.2 ± 0.1 at% (Fig. 9d). Additionally, the distribution of the Cu concentration measured in the two volumes is plotted to statistically compare it with a random distribution in Fig. 9c–d. Although there are small deviations for higher and lower concentrations visible, the distributions of the Cu concentration fit well to the random distribution.

4. Discussion

It is well known that differences in the strength of the alloying elements influence the deformation behavior during ball milling and lack of co-deformation in combination with low or no mutual solubility works against subsequent mechanical alloying [28,29,38–44]. Cordero et al. [29] recently studied the effects of phase strength mismatch in several W-transition metal couples during mechanical alloying by ball milling and experimentally showed that homogeneous solid solutions could only be obtained in W-transition metal couples having less than ~40% difference in strength. Furthermore, an asymmetric mixing kinetics – more W dissolved in the alloying element than vice versa-was observed. A kinetic Monte Carlo simulation, which was adapted to account for differences in phase strength in a model system, also reproduced the experimentally observed behaviors and was used to construct dynamical phase diagrams demonstrating the effects of composition and processing temperature on the formation of solid solutions during mechanical alloying.

This study focuses on Cu–Co composites, which have a dual-phase microstructure and a phase strength mismatch of ~70–80% in the initial state, if the indentation hardness of the individual Cu and Co phase is considered (Table 1, Fig. 6b). Comparing the hardness of the Cu and Co phase in the Cu–Co composites in the as-fabricated, initial condition [32,37], it yields a similar difference of ~75%. Estimating the yield stress by using the Tabor relation [48] gives thus a high yield stress difference between the Cu and Co phases and the assumption that a very hard, brittle phase (Co) is combined with a relatively soft, deformable phase (Cu) seems valid. Additionally, it might be expected that the dual phase structure of the composite maintains after using a different SPD process, namely HPT deformation, as well. However, experimental data from the correlative APT and TEM analysis of this study (Fig. 9) together with results of [32] strongly suggests that Cu- or Co-rich supersaturated solid solutions are formed at high applied strains after HPT processing over the whole investigated composition range.

Structural investigations in combination with the indentation hardness results further show that the deformation and mechanical mixing process is a multi-stage process, which is schematically illustrated in Fig. 10 and described in the following.

4.1. Stage A

From the microstructural observations (Fig. 2 and [32]) it is evident that the Cu phases are carrying more deformation than the Co phases due to the initial high hardness difference in all three investigated composites. Hence, plastic deformation is mainly localized in the softer Cu phases at low strain, which represents stage A. Microstructural refinement similar as in single-phase HPT deformed materials [49] predominately take place in the Cu phases. The Co phases, however, show some deformability in the beginning of the deformation process as well, which is more pronounced in the Co-rich composites. Grain refinement in the Cu phase originates from dislocation activities during deformation. At this stage, the Cu–Co interphase act as conventional barrier for dislocation motion. The main hardening mechanisms in the Cu and to a small, almost negligible extent also in the Co phase, are work-hardening and Hall-Petch hardening due to the grain refinement. The formation of a {111} texture is usually observed in pure Cu after HPT deformation [50]. Since the Co phase show less deformability, the formation of a pronounced texture in the Co phase might not occur. For Co grains or particles with a size below 100 nm, the continuous accumulation of stacking faults might further already lead to hcp-fcc phase transformations for very small grains at this stage [51].

The described processes of stage A lead to the first overall, strong microhardness increase of the composites, which shows a clear dependence on the volume fraction of Co (dashed lines in Fig. 4b). From the measurement of the indentation hardness of the Cu phase at the lowest applied strain ($\varepsilon = 5$ and 10) it can be further seen that hardening of the Cu phase in stage A is highest for the Cu phase in the Co-rich composite and decreases with decreasing phase fraction of Co (c.f. Table 1 and Fig. 6a).

Due to the heterogeneous deformation of the Cu–Co composites (Fig. 2), where deformation is predominantly carried by the Cu-phase, the local strain in Cu is larger compared to the applied strain and scales with the Co-content. For a simple composite model (layer model, where only the Cu phase/layer is deformed plastically), the local shear strain γ_{local} in the Cu phase can be estimated by

$$\gamma_{local} \cong \frac{t_{tot}}{t_{Cu}} * \gamma_{applied} \approx \frac{1}{1 - x_{Co}} \gamma_{applied}, \quad (1)$$

with t_{Cu} being the virtual Cu layer thickness and t_{tot} the total HPT sample thickness. $\gamma_{applied}$ is the applied shear strain during HPT deformation, which can be calculated from the applied equivalent strain ε ($\gamma_{applied} = \varepsilon^* \sqrt{3}$) [52]. As the molar weight of Cu and Co is very similar (63.5 and 59 g/mol, respectively) as well as the density

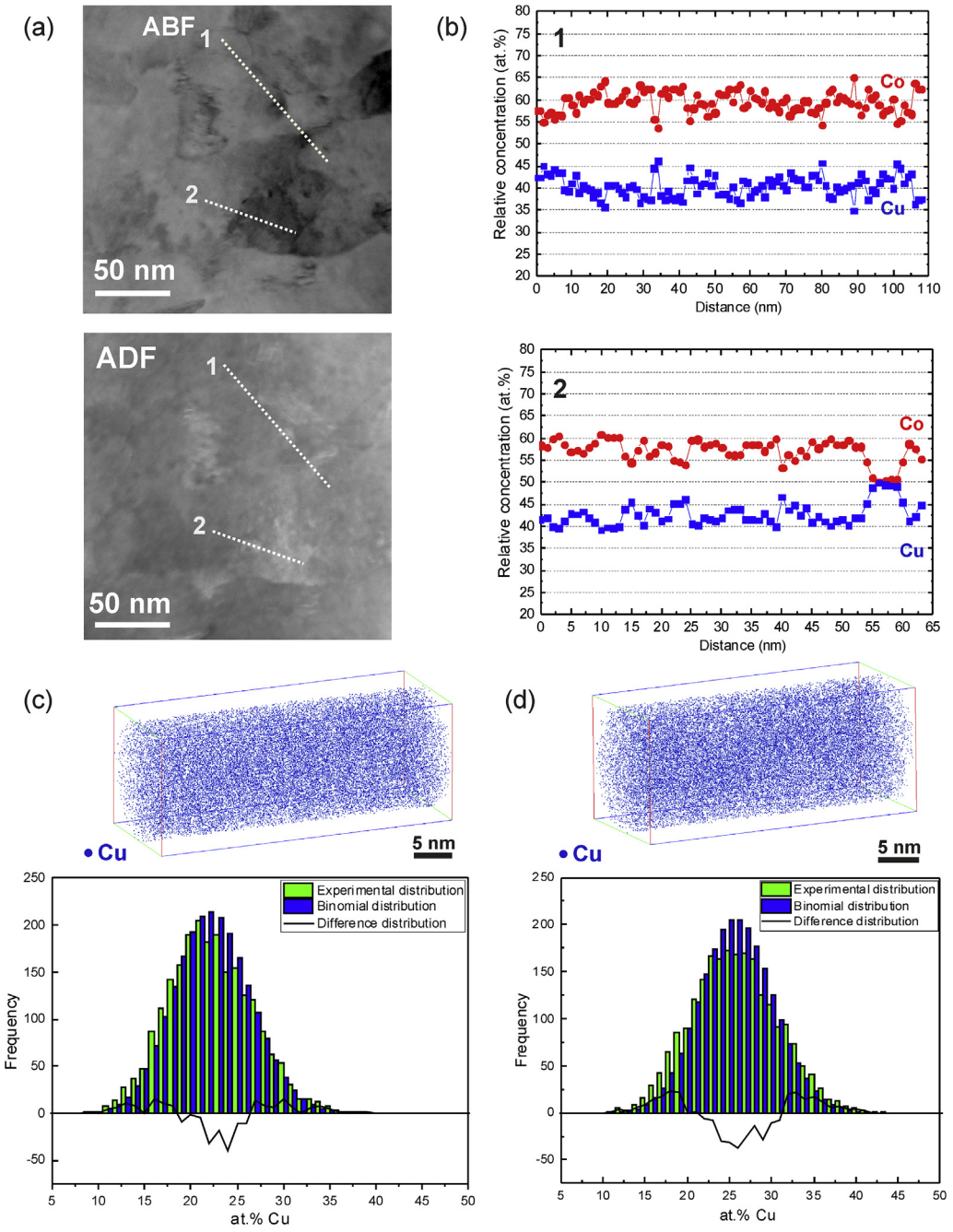

Fig. 9. (a) ABF and ADF STEM image of the Cu-54 at.%Co composite at an applied strain of 440. (b) EELS concentrations profiles in atomic percent for Cu and Co along the line 1 and line 2 drawn in (a). (c)–(d) Three-dimensional reconstructions of two volumes analyzed by APT in the Cu-76 at.%Co composite at an applied strain of 430 (the reconstructions are taken from two different APT specimens). Only Cu atoms are displayed to show their homogeneous distribution in the analyzed volumes. The corresponding Cu frequency distributions from the displayed volumes compared to a random distribution are also shown.

(~8.9 g/cm^3 for both), the thickness t_{Cu} can be directly related to the Cu content in at% (x_{Cu} = 1-x_{Co}). Hence, the local strain in the Cu phase is assumed to increase from 33% over 50% to 300% compared to the applied strain for the Cu-26 at.%Co, -54 at.%Co and -76 at.%Co composite, respectively, and correlates quite well with the slope of the initial hardness increase (Fig. 4a). Furthermore, due to the strong strain localization, the local strain gradient present by the torsional loading is further increased and additionally enhanced by the phase boundaries [53,54]. In fact, strain gradients are inversely proportional to an internal material length scale over which plastic deformation occur [55,56], which is in a first order approximation equal to the phase spacing or the lamellar distance of the Cu or Co phase in this work. Hence, higher strain gradients and strains evolve in the Cu phases as the volume fraction of the hard, less deformable Co phase increases which are highest in the Cu phase of the Cu-76 at.%Co composite. Both effects lead to an increased work hardening and microstructure refinement and explain the additional hardening of the Cu phase with increasing volume fraction of the Co phase during stage A and the subsequent stage B (medium applied strains) as described in the following.

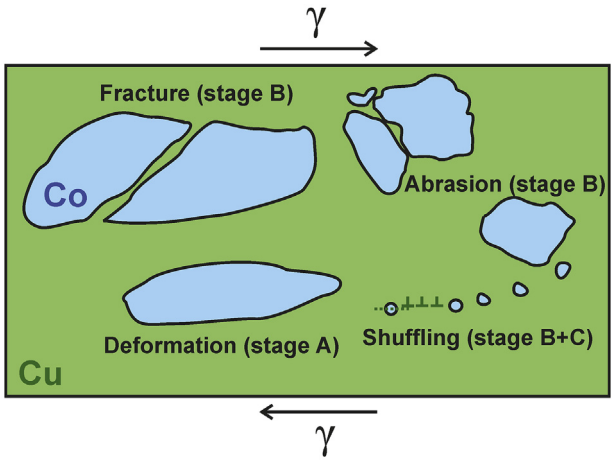

Fig. 10. Schematic representation of the multi-stage deformation and mechanical mixing process of the Cu–Co composites during HPT deformation.

4.2. Stage B

At medium applied strains (stage B), the tendency to fragment predominates over the plastic deformation of the Co phase. During the HPT deformation, all samples deform homogeneously at the macroscopic scale. The Cu phase is therefore continuously sheared. Co particles, however, continue to fragment and fracture, and simultaneously collide over and over again during ongoing HPT deformation. This is in particular true for the Co-rich composites with a high fraction of Co. If two Co particles collide, small Cu fragments can be formed, which might then be trapped inside the Co phase. Small Cu fragments can indeed be found within the Co phase (Fig. 8a). Behind the Cu fragment, an enhanced Cu concentration is measured in the Co phase, which could be interpreted as traces of abrasion of Cu. On the contrary, no Cu dissolved in the Co phase can be found right between the Cu fragment and the Cu phase boundary (Fig. 8a). Furthermore, it is shown, that Cu phase regions with nearly no dissolved Co atoms are simultaneously observed (Fig. 8a). Mechanical alloying is, however, not limited to the Cu phase. Nanometer sized small Co particles may also fracture from edges of the Co particles. In Fig. 8b–c, nanometer sized small fragments of Co are clearly visible inside the Cu phase. The shape of these fragments is elongated, which indicates further deformation of the tiny fragments. Due to the similarity of the fragmentation/fracture process of the Co phase and the abrasion of the Cu phase by the hard Co particles with abrasive processes like abrasive machining, stage B is called “fracture” and “abrasion” (Fig. 10).

In stage B, the hardening capability of the soft phase (Cu) is most important. Fracturing and fragmentation of the Co particles is enhanced if the strength or the hardness of the Cu phase increases. Both Co-rich composites display a larger amount of hardening compared to the Cu-26 at.%Co composite if the relative increase in microhardness is considered (Fig. 4). The use of the nano-indentation measurements in this work, however, enable to directly follow the evolution of the hardness of the Cu phase as function of increasing applied strain, which is indeed much higher in the Co-rich composites (Table 1, Fig. 6a). Additionally, the time required to reach the steady state (defined by a homogeneous microstructure and indentation hardness) depends on the Co content (Figs. 5 and 7).

The fragmentation and fracturing process might be also supported by plastic instabilities. On the mesoscopic scale, such instabilities can be caused by strain localization and the possible formation of localized deformation bands, cutting particles and hence support their fragmentation and fracturing. On the other hand, microscopic plastic instabilities of thin rods and plates as described in Refs. [57–59] might also occur. These instabilities are important on a smaller length scale, especially for very fine, nanometer-sized filaments as can be seen in Figs. 2h and 3h–i, for instance. Studies on such stress driven instabilities of interfaces in solids show that the instability condition depends on the relative magnitude of the applied and/or misfit strains, the elastic mismatch α and the volume fraction of both phases [58]. For an external applied strain, the interface of lamellar (plate-like) and fibrous (rod-like) composites is always unstable for all $\alpha \neq 0$. Once plastic instabilities set in, surface fluctuations or undulations are formed. The critical wavenumber, the maximally unstable wavenumber and the instability growth rate are, for example, all increased for rod-composite structures with a $\alpha \neq 0$. In addition, the time required for destabilization (spherodization) is substantially reduced by application of an external stress [58]. With ongoing deformation, the Co particles continue to reduce in size, wear and become more and more rounded by the aforementioned processes. As a consequence, the fragmentation and fracture probability decrease with decreasing size and circularity of the Co particles. In addition, Co particles with round edges are much less effective for the abrasion process.

Atomic scale processes like defect-enhanced diffusion [60–63] and the dislocation shuffling process [64] might be responsible for final phase dissolution. While the former process can occur for larger particles as well, the latter may play an important role for the dissolution of the nanoscaled Co particles as well as the Cu fragments trapped inside Co with nanometer sized phase dimensions. As the Cu and Co phase are deformed, the defect density (vacancies, dislocations) in both phases increase and Co atoms at the interface might diffuse into the Cu phase and vice versa. In the dislocation shuffling process, atomic planes are sheared through dislocation glide on more than one slip system across heterophase interfaces [64]. Hence, tiny Co material portions in Cu and vice versa are created, which are subsequently cut by dislocations running through them [64]. A necessary condition is an allotropic phase transformation from hcp Co to fcc Co, which is reported in literature for small Co grains (<100 nm) and which might also occur for the tiny, nanometer-sized Co particles during stage B [51]. At the highest applied deformation strain, evaluation of selected area diffraction patterns display only fcc diffraction rings for all composites regardless their composition. Hence, even in the Co-rich composite, the formation of a supersaturated fcc Co solid solution takes place. Phase transformation of hcp Co to fcc Co, promoting the dissolution of small Co particles and Cu fragments by the dislocation shuffling process and subsequent short range diffusion processes, may therefore certainly possible.

A tendency for asymmetric mixing, similar as observed in mechanical alloying of powders with a high strength difference [29], might be present in the Co-rich composites as well. On the one hand, the “fracture and abrasive” processes (Fig. 10) is asymmetric itself. The Co phase fragment, fracture and continuously decrease in size, whereas the Cu phase retains its phase dimensions and is predominately deformed. This leads to a quite fine dispersion of small-sized Co particles in the Cu matrix, which are then dissolved in the Cu finally by defect-enhanced diffusion or a dislocation shuffling process. As the Cu phase is predominantly deformed (especially in the early stages of the HPT process) the defect density in this phase will increase to a larger extent. Hence an imbalance in the defect density between the Cu and Co phases will arise, which will lead to an asymmetry in the diffusion fluxes at the interface: more Co atoms will diffuse into the defect-rich Cu phase as vice versa [63]. Furthermore, the solubility of Co in Cu can be increased by a high vacancy density. This process is likely to occur already in

stage B (Fig. 10) and might be one reason for the continuously increasing hardness of the Cu phase. If both phases are soft (or hard) the strain distribution is more homogeneous and no asymmetry would be expected from this mechanism. The dislocation shuffling process is asymmetric as well. Embury et al. [40] defined several criteria that promote heterophase slip transfer, which is an important step of the dislocation shuffling process [64]. One criteria is that the misorientation between active slip planes on both side of the heterophase boundary should be a minimum at the boundary. Another one is that the configuration of the interface should also be one of minimum energy. Hence, the dislocation shuffling process is dependent on the type of interface too. This leads also to an asymmetry in the mixing process.

It is further assumed that mechanical mixing by the above described atomic scale processes start right after stage A. In spite of being a rough estimate, a decrease of the phase fraction of the respective alloying element is visible for all composite (Fig. 4b). Alloying with Co induces additional hardening of the Cu phases due solid solution strengthening and further grain size refinement as direct consequence of alloying [49]. Results from the APT measurements of the Cu-76 at.%Co composite (Fig. 8), in which up to 30 at.% Co are dissolved in the Cu phase, further strengthen the assumption that the intermixing already starts at medium applied strains ($\varepsilon = 30$). However, it should be noted that the local shear strain in the Cu phase might be considerable enhanced according to equation (1).

Dissolution of small Co particles and Cu fragments steadily continue through stage B and stage C, which will be further described in the following.

4.3. Stage C

The final stage of the HPT deformation process (stage C) is characterized by a diminishing phase strength mismatch (Fig. 6). Once the indentation hardness (or the yield stress) of the Cu and Co phase becomes more similar, deformation of both phases becomes more uniform and the formation of homogeneous solid solutions is strongly promoted and accelerated.

Phase strength differences are quickly reduced in the Co-rich composites (Fig. 6). In the Cu-54 at.%Co composite, a rather homogeneous indentation hardness with only small hardness differences (~30%) is reached at an applied strain of 110. In the Cu-76 at.% Co composite, similar indendation hardness differences and subsequent structural homogenization are obtained at slightly higher applied strains ($\varepsilon = 140$). Areas with smaller hardness difference can, however, be found at a smaller applied strains, too (c.f. hardness along line L2 at $\varepsilon = 100$ in Fig. 7c with a difference of 32%). The relative hardness of the Cu-54 at.%Co composite is slightly higher compared to the Cu-76 at.%Co composites in the steady state of HPT deformation (Fig. 4a). The hardness in the steady state is governed by the small structural size of the grains (grain boundary strengthening), work-hardening and solid solution hardening. For substitutional solutions, the yield strength increases in proportion to their concentration of solutes and the strengthening as a function of the concentration c of the solute in an alloy can be obtained from different models [65,66]. Not only solid solution formation proceeds fastest in the Cu-54 at.%Co composite, the amount of the solid solution hardening contribution to the overall hardness is highest, too.

In general, HPT deformed bulk Cu and Co [35,36] or HPT deformed Cu and Co powders [22,36] obtain a different saturation hardness ($HV_{Cu} < HV_{Co}$) in the steady state of HPT deformation. Hence, Cu has a smaller saturation hardness compared to Co if pure HPT deformed Cu and Co materials are considered. Regarding the Cu–Co composites, Co in solid solution generally strengthen the Cu phase [65,66]. Alloying Cu with Co further lowers the stacking fault energy of Cu [67]. Hence, the increasing difficulty to cross-slip with decreasing stacking fault energy (and, therefore, the difference in the ease of dynamic recovery) is believed to increase the work hardening rate of the Cu phase dependent on the amount of Co which is dissolved in Cu. Fig. 6a displays the indentation hardness of the Cu phase as a function of the applied strain. Hardening of the Cu phase is by far the lowest for the composite with the lowest amount of Co. Although more than one strengthening mechanisms simultaneously occur, the measured indentation hardness of the Cu phase might be taken as a rough estimate of the influence of Co in solid solution on the hardening and on the strain hardening of Cu.

Due to the limited hardening ability of the Cu phase in Cu-26 at.%Co composite, the dissolution of the Co phase progresses very slowly and high phase strength differences are maintained until high applied strains (c.f. Figs. 5 and 7). As a consequence, the formed solid solution is not entirely homogenous and few, very small Co particles remain in the Cu-26 at.%Co composite even at the highest applied strain [32]. Since small particles are completely dissolved by dislocation shuffling and defect enhanced diffusion and co-deformation sets in, no further hardening is observed in stage C and the composites behave like single phase material in the saturation or steady-state region [49].

4.4. Final remarks

From the present results of the structural and mechanical characterization, the critical indentation hardness or yield strength mismatch for the beginning of co-deformation can be determined to be about 30% (Fig. 6b), which is quite consistent with the findings in Ref. [29]. In the Cu-26 at.%Co composite, this critical strength mismatch is never reached (at least for the deformation strains applied in this work). However, it has been shown that an extended solubility of Co in fcc Cu for applied strains of about 100 and higher can be obtained in the Cu-rich composite [32]. Thus it can be concluded that the mechanical alloying process during HPT deformation already starts at medium applied strains (stage B), even before pronounced co-deformation of both phases starts. This is further confirmed by the results of two APT measurements of the Cu-76 at.%Co composite at low applied strains (Fig. 8). Moreover it is important to note that even in the case of the Cu-26 at.%Co composite, the formation of homogeneous supersaturated solid solutions might be achievable although very high applied strains would be needed to reach a homogenous single-phase solid solution. A further requirement to achieve a single phase microstructure in the Cu-rich composite is that no instable deformation localization (e.g. shear banding, cracking) occurs at higher applied strains. Strain localization and shear banding is, for example, observed in Cu–Ag alloys processed by HPT after a certain amount of strain is applied (ε~50) [24]. Although the Cu and Ag phases are both ductile and have comparable strengths, initial co-deformation is replaced by this localized deformation at higher applied strains, which inhibits the formation of homogeneous single-phase solid solutions and leads to a final microstructure composed of single- and two-phase regions for medium compositions [24]. Taking into account the present results of the Cu-rich composite for an applied strain up to 430, such strong strain localization is not expected to occur at higher applied strains in the current alloy system.

Considering all results together, we conclude that not only the initial phase strength mismatch is significant for mechanical alloying during HPT deformation, but also the hardening behavior of the individual phases. In the composite type “ductile-brittle”, like the investigated Cu–Co composites, the hardening capability of the soft phase is particularly important. Furthermore, the SPD process itself might have a considerable significance to achieve alloying in a

"ductile-brittle" type of composites. During SPD deformation, a large hydrostatic pressure is applied and no significant change of the overall dimensions of the sample during processing occurs [2–4]. The Cu and Co phase, although deforming inhomogenously, are continuously sheared or fragmented and fractured during HPT processing promoting the dissolution of the respective phase into the other phase of the composite. In contrast, powder particles during mechanical alloying are repeatedly changing their size and form by being repeatedly flattened, cold welded, fractured and rewelded only for a certain milling time until a steady-state is attained [27]. For "ductile-brittle" powder combinations, it has been frequently observed that the brittle particles are initially fragmented and, if they are insoluble, tend to become trapped in the ductile particles after a while. The outcome after continued milling is a uniform dispersion of the brittle particles in the ductile component of the composite without significant alloying in immiscible components [26,27,30].

5. Conclusion

In this study, bulk mechanical alloying of dual-phase Cu-Co composites by HPT deformation is investigated. The results are summarized as follows:

During HPT deformation, supersaturated solid solutions can be obtained in the Cu–Co composites, regardless of their initial composition and their high initial yield strength difference . The deformation and mechanical alloying process can be divided into different stages: In the beginning, plastic deformation is mainly localized in the softer Cu phases. Work-hardening, grain size strengthening due to microstructural refinement and alloying together with solid solution hardening induce higher hardness of the Cu phases in the composites. The hardening ability of the Cu phase further depends strongly on the composition and the thus induced strain gradients, being highest for the composite with the highest volume fraction of the hard Co phase. Uniform deformation progresses significantly as the hardness difference of the evolving Cu and Co phase become smaller. Co-deformation, which is the last stage of the deformation process, starts, if less than 30% indentation hardness difference is reached, and leads to further intermixing and formation of homogeneous solid solutions in the Co-rich composites. However, mechanical mixing is already observed in the Co-rich composite before massive co-deformation sets in and is furthermore also observed in the Cu-rich composite, in which the critical phase strength difference is not even reached at the highest applied strain. Hence, co-deformation is not a necessary condition for the formation of supersaturated solid solutions, but facilitate and accelerate mixing during HPT deformation. Additionally, mechanical mixing, which seems to occur by an abrasive-like process, takes place in the hard Co phase of the Co-rich composite as well.

Acknowledgements

The authors gratefully acknowledge the financial support by the Austrian Science Fund (FWF): J3468-N20. The atom probe instrument and scanning electron microscope was financed by the DFG and the Federal State Government of Saarland (INST 256/298-1 FUGG, INST 256/340-1 FUGG). We thank E. Arzt for his support through INM.

Appendix A. Supplementary data

Supplementary data related to this article can be found at http://dx.doi.org/10.1016/j.actamat.2016.06.010.

References

[1] D.L. Leslie-Pelecky, R.D. Rieke, Magnetic properties of nanostructured materials, Chem. Mater. 8 (1996) 1770–1783.
[2] R. Valiev, Nanostructuring of metals by severe plastic deformation for advanced properties, Nat. Mater. 3 (2004) 511–516.
[3] R.Z. Valiev, M.J. Zehetbauer, Y. Estrin, H.W. Höppel, Y. Ivanisenko, H. Hahn, G. Wilde, H.J. Roven, X. Sauvage, T.G. Langdon, The innovation potential of bulk nanostructured materials, Adv. Eng. Mater. 9 (2007) 527–533.
[4] R.Z. Valiev, R.K. Islamgaliev, I.V. Alexandrov, Bulk nanostructured materials from severe plastic deformation, Prog. Mater. Sci. 45 (2000) 103–189.
[5] G. Wilde, H. Rösner, Stability aspects of bulk nanostructured metals and composites, J. Mater. Sci. 42 (2007) 1772–1781.
[6] S. Ohsaki, S. Kato, N. Tsuji, T. Ohkubo, K. Hono, Bulk mechanical alloying of Cu–Ag and Cu/Zr two-phase microstructures by accumulative roll-bonding process, Acta Mater 55 (2007) 2885–2895.
[7] X. Sauvage, P. Jessner, F. Vurpillot, R. Pippan, Nanostructure and properties of a Cu-Cr composite processed by severe plastic deformation, Scr. Mater. 58 (2008) 1125–1128.
[8] A. Bachmaier, M. Kerber, D. Setman, R. Pippan, The formation of supersaturated solid solutions in Fe–Cu alloys deformed by high-pressure torsion,, Acta Mater. 60 (2012) 860–871.
[9] H. Shen, Z. Li, B. Günther, A.V. Korznikov, R.Z. Valiev, Influence of powder consolidation methods on the structural and thermal properties of a nanophase Cu-50wt%Ag alloy, Nanostruct. Mater. 6 (1995) 385–388.
[10] B.B. Straumal, A.R. Kilmametov, Y. Ivanisenko, L. Kurmanaeva, B. Baretzky, Y.O. Kucheev, P. Zięba, A. Korneva, D.A. Molodov, Phase transitions during high pressure torsion of Cu–Co alloys, Mater. Lett. 118 (2014) 111–114.
[11] U. Czubaykoa, N. Wanderkaa, V. Naundorfa, V.A. Ivchenkob, A. Ye Yermakovc, M.A. Uiminc, H. Wollenberger, Three-dimensional atom probing of supersaturated mechanically alloyed Cu–20at.% Co, Mater. Sci. Eng. A 327 (2002) 54–58.
[12] C. Gente, M. Oehring, R. Bormann, Formation of thermodynamically unstable solid solutions in the Cu–Co system by mechanical alloying, Phys. Rev. B 48 (1993) 13244–13252.
[13] C.L. Chien, S.H. Liou, D. Kofalt, W. Yu, T. Egami, T. McGuire, Magnetic properties of FexCu100–x solid solutions, Phys. Rev. B 33 (1986) 3247–3250.
[14] J.R. Childress, C.L. Chien, Reentrant magnetic behavior in fcc Co-Cu alloys, Phys. Rev. B 43 (1991) 8089–8093.
[15] B.D. Krack, V. Ozolins, M. Asta, I. Daruka, "Devil's staircases" in bulk-immiscible ultrathin alloy films, Phys. Rev. Lett. 81 (2002) 186101.
[16] T. Aizawa, T. Zhou, Nanogranulation process into magneto-resistant Co–Cu alloy on the route of bulk mechanical alloying, Mater. Sci. Eng. A 285 (2000) 1–7.
[17] K. Suehiro, S. Nishimura, Z. Horita, Change in magnetic property of Cu–6.5 mass%Co alloy through processing by ECAP, Mater. Trans. 49 (2008) 102–106.
[18] B.B. Straumal, S.G. Protasova, A.A. Mazilkin, B. Baretzky, D. Goll, D.V. Gunderov, R.Z. Valiev, Effect of severe plastic deformation on the coercivity of Co–Cu alloys, Philos. Mag. Lett. 89 (2009) 649–654.
[19] Y. Nakamoto, M. Yuasa, Y. Chen, H. Kusuda, M. Mabuchi, Mechanical properties of a nanocrystalline Co–Cu alloy with a high-density fine nanoscale lamellar structure, Scr. Mater. 58 (2008) 731–734.
[20] A.E. Berkowitz, J.R. Mitchell, M.J. Carey, A.P. Young, S. Zhang, F.E. Spada, F.T. Parker, A. Hütten, G. Thomas, Giant magnetoresistance in heterogeneous Cu–Co alloys, Phys. Rev. Lett. 68 (1992) 3745–3748.
[21] J. Wecker, R. von Helmolt, L. Schultz, K. Samwer, Giant magnetoresistance in melt spun Cu–Co alloys, Appl. Phys. Lett. 62 (1993) 1985–1987.
[22] A. Bachmaier, M. Pfaff, M. Stolpe, H. Aboulfadl, C. Motz, Phase separation of a supersaturated nanocrystalline Cu–Co alloy and its influence on thermal stability, Acta Mater. 96 (2015) 269–283.
[23] X. Sauvage, G. Wilde, G.P. Dinda, Non-equilibrium intermixing and phase transformation in severely deformed Al/Ni multilayers, Scr. Mater. 56 (2006) 181–184.
[24] K.S. Kormout, B. Yang, R. Pippan, Deformation behavior and microstructural evolution of Cu–Ag alloys processed by high-pressure torsion, Adv. Eng. Mater. 17 (2015) 1828–1834.
[25] I. Sabirov, R. Pippan, Characterization of tungsten fragmentation in a W-25% Cu composite after high-pressure torsion, Mater. Charact. 58 (2007) 848–853.
[26] J.S. Benjamin, T.E. Volin, The mechanism of mechanical alloying, Metall. Trans. 5 (1974) 1929–1934.
[27] C. Suryanarayana, Mechanical alloying and milling, Prog. Mater. Sci. 46 (2001) 1–184.
[28] J. Xu, G.S. Collins, L.S.J. Peng, M. Atzmon, Deformation-assisted decomposition of unstable Fe50Cu50 solid solution during low-energy ball milling, Acta Mater. 47 (1999) 1241–1253.
[29] Z.C. Cordero, C.A. Schuh, Phase strength effects on chemical mixing in extensively deformed alloys, Acta Mater. 82 (2015) 123–136.
[30] P.S. Gilman, J.S. Benjamin, Mechanical alloying, Annu. Rev. Mater. Sci. 13 (1983) 279–300.
[31] R.M. Davis, C.C. Koch, Mechanical alloying of brittle components: silicon and germanium, Scr. Metall. 21 (1987) 305–310.
[32] A. Bachmaier, H. Aboulfadl, M. Pfaff, F. Mücklich, C. Motz, Structural evolution and strain induced mixing in Cu-Co composites studied by transmission electron microscopy and atom probe tomography, Mater. Character 100

(2015) 178–191.
[33] N.J. Simon, E.S. Drexler, R.P. Reed, National Institute of Standards and Technology Monograp 177: Properties of Copper and Copper Alloys at Cryogenic Temperatures, Washington, 1992.
[34] C.C. Sanderson, Deformation of Polycrystalline Cobalt, University of British Columbia, 1965. PhD thesis.
[35] N. Lugo, N. Llorca, J.M. Cabrera, Z. Horita, Microstructures and mechanical properties of pure copper deformed severely by equal-channel angular pressing and high pressure torsion, Mater. Sci. Eng. A 477 (2008) 366–371.
[36] A. Bachmaier, C. Motz, On the remarkable thermal stability of nanocrystalline cobalt via alloying, Mater. Sci. Eng. A 624 (2015) 41–51.
[37] A. Bachmaier, E. Neubauer, M. Kitzmantel, R. Pippan, C. Motz, Microstructural evolution in immiscible alloys processed by high-pressure torsion, IOP Conf. Ser. Mater. Sci. Eng. 63 (2014) 012023.
[38] Y. Ashkenazy, N.Q. Vo, D. Schwen, R.S. Averback, P. Bellon, Shear induced chemical mixing in heterogeneous systems, Acta Mater. 60 (2012) 984–993.
[39] L.B. Hong, B. Fultz, Two-phase coexistence in Fe-Cu alloys synthesized by ball milling, Acta Mater. 46 (1998) 2937–2946.
[40] C.W. Sinclair, J.D. Embury, G.C. Weatherly, Basic aspects of the co-deformation of bcc/fcc materials, Mater. Sci. Eng. A 272 (1999) 90–98.
[41] S. Odunuga, Y. Li, P. Krasnochtchekov, P. Bellon, R.S. Averback, Forced chemical mixing in alloys driven by plastic deformation, Phys. Rev. Lett. 95 (2005) 04590.
[42] N.Q. Vo, R.S. Averback, Y. Ashkenazy, P. Bellon, J. Wang, Forced chemical mixing at Cu-Nb interfaces under severe plastic deformation, J. Mater. Res. 27 (2012) 1621–1630.
[43] N.Q. Vo, J. Zhou, Y. Ashkenazy, D. Schwen, R.S. Averback, P. Bellon, Atomic mixing in metals under shear deformation, JOM 65 (2013) 382–389.
[44] Q.V. Nhon, S. Odunuga, P. Bellon, R.S. Averback, Forced chemical mixing in immiscible alloys during severe plastic deformation at elevated temperatures, Acta Mater. 57 (2009) 3012–3019.
[45] N.X. Randall, M. Vandamme, F.J. Ulm, Nanoindentation analysis as a two-dimensional tool for mapping the mechanical properties of complex surfaces, J. Mater. Res. 24 (2009) 679–690.
[46] K. Thompson, D. Lawrence, D.J. Larson, J.D. Olson, T.F. Kelly, B. Gorman, In situ site-specific specimen preparation for atom probe tomography, Ultramicroscopy 107 (2007) 131–139.
[47] P. Bas, A. Bostel, D. Blavette, A general protocol for the reconstruction of 3D atom probe data, Appl. Surf. Sci. 87/88 (1995) 298–304.
[48] G. Tabor, The Hardness of Metals, Clarendon Press, Oxford, 1951.
[49] R. Pippan, S. Scheriau, A. Taylor, M. Hafok, A. Hohenwarter, A. Bachmaier, Saturation of fragmentation during severe plastic deformation, Annu. Rev. Mater. Sci. 40 (2010) 319–343.
[50] H. Jiang, Y.T. Zhu, D.P. Butt, I.V. Alexandrov, T.C. Lowe, Microstructural evolution, microhardness and thermal stability of HPT-processed Cu, Mater. Sci. Eng. A 290 (2000) 128–138.
[51] G.P. Zheng, Y.M. Wang, M. Li, Atomistic simulation studies on deformation mechanism of nanocrystalline cobalt, Acta Mater. 53 (2005) 3893–3901.
[52] H.P. Stüwe, Equivalent strains in severe plastic deformation, Adv. Eng. Mater. 5 (2003) 291–295.
[53] M.F. Ashby, The deformation of plastically non-homogeneous materials, Phil. Mag. 21 (170) (1970) 399–424.
[54] J.F. Nye, Some geometrical relations in dislocated crystals, Acta Metall. 1 (1953) 153–162.
[55] N.A. Fleck, J.W. Hutchinson, A phenomenological theory for strain gradient effects in plasticity, J. Mech. Phys. Solid 41 (12) (1993) 1825–1857.
[56] V.P. Smyshlyaev, N.A. Fleck, Bounds and estimates for linear composites with strain gradient effects, J. Mech. Phys. Solids 42 (1994) 1851–1882.
[57] J. Colin, L. Thilly, F. Lecouturier, J.P. Peyrade, S. Askénazy, J. Grilhé, Axial and radial interface instabilities of copper/tantalum cylindrical conductors, Acta Mater. 47 (1999) 2761–2768.
[58] N. Sridhar, J.M. Rickman, D.J. Srolovitz, Microstructural stability of stressed lamellar and fiber composites, Acta Mater. 45 (1997) 2715–2733.
[59] N. Sridhar, J.M. Rickman, D.J. Srolovitz, Multilayer film stability, J. Appl. Phys. 82 (1997) 4852–4859.
[60] J. Eckert, J.C. Holzer, W.L. Johnson, Thermal stability and grain growth behavior of mechanically alloyed nanocrystalline Fe-Cu alloys, J. Appl. Phys. 73 (1993) 131–141.
[61] J. Eckert, J.C. Holzer, C.E. Krill III, W.L. Johnson, Reversible grain size changes in ball-milled nanocrystalline Fe–Cu alloys, J. Mater. Res. 8 (1992) 980–1983.
[62] E. Ma, H.W. Sheng, J.H. He, P.J. Schilling, Solid-state alloying in nanostructured binary systems with positive heat of mixing, Mater. Sci. Eng. A 286 (2000) 48–57.
[63] R.B. Schwarz, Microscopic model for mechanical alloying, Mater. Sci. Forum 269–272 (1998) 665–674.
[64] D. Raabe, S. Ohsaki, K. Hono, Mechanical alloying and amorphization in Cu–Nb–Ag in situ composite wires studied by transmission electron microscopy and atom probe tomography, Acta Mater 57 (2009) 5254–5263.
[65] R. Labusch, A statistical theory of solid solution hardening, Phys. Status Solidi A 41 (1970) 659–669.
[66] R. Labusch, Statistische theorien der mischkristallhärtung, Acta metall. 20 (1972) 917–927.
[67] F.W. Gayle, F.S. Biancaniello, Stacking faults and crystallite size in mechanically alloyed Cu-Co, Nanostruct. Mater. 6 (1995) 429–432.